

Design, Modeling and Control of a SMA-Actuated Biomimetic Robot with Novel Functional Skin

Joan Ortega Alcaide, Levi Pearson, and Mark E. Rentschler, Member, IEEE

Abstract—Traditional colonoscopy requires highly trained personnel to be performed. Additionally, current devices may cause discomfort and carry the risk of perforating the bowel wall. In this paper, a soft three modular section robot is designed, modeled, controlled and tested. Each of the robotic sections has three degrees of freedom, one translation and two rotations. The robot uses a peristaltic motion to translate, inspired by the motion generated by the bowel. The robot uses nine independently controlled Shape Memory Alloy (SMA) springs as its actuators and a novel silicone rubber skin provides the passive recovery force to expand the springs to their original state. It also incorporates three air tubes, one for each section, to provide forced convection reducing the cooling time of the SMA springs. A parametric study on the skin curvature and thickness using Finite Element Analysis (FEA) is performed to maximize traction while providing enough recovery force. A multi-input multi-output (MIMO) controller based on fuzzy control is designed and implemented for each of the sections allowing the robot to achieve any orientation between -90° and $+90^\circ$ in both pitch and roll in less than 4 seconds with near zero steady state error. Both the peristaltic motion and the orientability of the robot are tested. The robot is able to perform a peristaltic motion with maximum speed of 4 mm/s (24 cm/min) and an average speed of 2.2 cm/min. Each section is also able to follow, with less than 2% overshoot and near zero steady-state error, periodic multi-input squared signals of 25° of amplitude.

I. INTRODUCTION

Currently a number of gastrointestinal diseases such as inflammatory bowel disease and colon cancer require a colonoscopy to be accurately diagnosed. Specifically, colon cancer is the third most deadly cancer in United States, both for men and women [1]. An early detection of precancerous, or potentially cancerous polyps is essential for a successful recovery [1].

Traditional colonoscopy uses a flexible scope with a camera and a tool port to explore the large bowel. Colonoscopy is a technically challenging procedure that must be performed by a highly trained physician [2]. In addition, it may produce discomfort and carries the risk of colon perforation [3]. An automated, reduced-risk approach would eliminate the need for highly trained operators and could improve patient comfort and safety. Therefore, the procedure would be more accessible and comfortable to people, helping to increase screening rates and consequently improve early cancer detection.

Capsule endoscopy (CE) is a method that overcomes many of the stated limitations. Currently, the PillCam[®] Colon

J. Ortega Alcaide, L. Pearson and M. E. Rentschler are with the Department of Mechanical Engineering, University of Colorado, Boulder, CO 80309 USA (e-mail: Joan.OrtegaAlcaide-1@colorado.edu; levi.pearson@colorado.edu; mark.rentschler@colorado.edu).

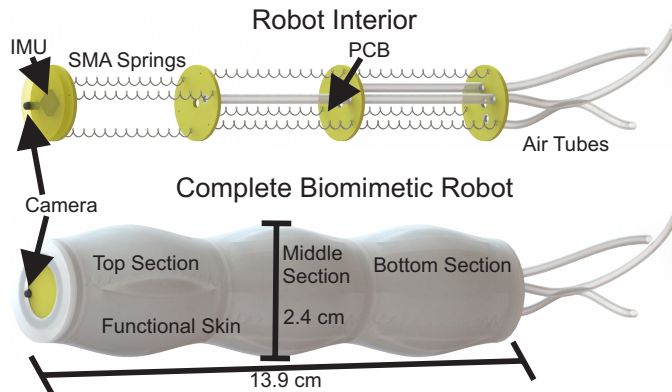


Fig. 1. Top: Computer-aided design of the interior of the biomimetic robot. Bottom: Computer-aided design of the complete biomimetic robot with its silicone rubber skin.

is the only commercially available capsule able to explore the large bowel. The PillCam[®] Colon is swallowed by the patient and passively moves through the gastrointestinal (GI) track transmitting images at a maximum rate of 35 frames per second. However, the lack of active control makes it difficult to determine location. In addition, there is the risk of capsule retention [4]. Also, if a possible cancerous or pre-cancerous tumor is detected, a colonoscopy is still required.

Many research groups are working on the development of an active device able to perform a colonoscopy [5], [6], [7], [8], [9]. These devices can be categorized as a function of the locomotion mechanism used. Magnetically driven capsules are being researched by Ciuti, G et al. [9], legged capsules have been developed by Kim, B et al. [10], a hybrid capsule combining both of the mechanisms was developed by Simi, M. et al. [11], treaded robots are being researched by Sliker, L et al. [5] and finally worm-like robots have been investigated by Wang, K et al. [12]. Here we present a modular, SMA-actuated robot with a novel functional skin. This soft robot utilizes a biomimetic peristaltic wave to translate.

II. ROBOT DESIGN

A three section biomimetic robotic worm is envisioned as the minimal design capable of conforming to the large bowel shape and of performing a peristaltic motion. In Figure 1 a general overview of this robot is presented. The robot consists of three identical sections. Each section has three SMA springs positioned at 120° of each other. The robot is enclosed by a novel soft silicone rubber skin (Ecoflex[®] 00-50). Each modular section is 4.6 cm long and 2.4 cm

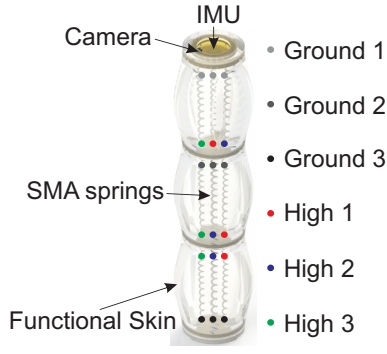


Fig. 2. Render of the complete three section soft robot displaying its main components: Functional Skin, SMA springs, Camera and IMU. In grey, the three independently controlled grounds and in red, blue and green the three independently controlled high voltage connections.

in diameter. The three SMA springs allow for the control of the orientation and extension of each of the sections. The soft skin is responsible for providing the recovery force to the SMA springs and conforming to, and interacting with, the bowel wall. Finally, the top section of the robot incorporates a 4 mm-wide camera (RS4018A-118, Bangu Technology Development Company Limited, Guangdong, China) and an Inertial Measurement Unit (IMU) (Inversense MPU-9150TM).

In each section, each SMA spring is independently controlled by means of a Pulsed Width Modulated (PWM) current signal [13]. A 5 V power supply (BK Precision[®] 1760A DC Power Supply) provides the necessary current. To minimize wires a matrix wire management approach is implemented [13]. As shown in Figure 2, each section has a common ground for the three springs, while the positive connections are shared between each of the columns. This allows for an independent control of the nine springs by means of just six 32 Ga electric wires. The PWM signal is provided by an Arduino Mega 2560 through a custom-made power board that transforms the data signal into a current signal by means of an H-bridge implemented with six Mosfets. The expansion of the SMA springs in their cold martensitic state is performed by the silicone rubber skin. In addition, to reduce the austenitic to martensitic phase transformation time, ambient air can be independently pumped into each of the sections through three valves (Solenoid Air Directional Control Valve, with 2 Ports, Single Solenoid, 10-32 UNF, 12V DC). The pumped air flows out of the robot through a 2 mm hole at the bottom platform of the robot. In this work, the SMA springs and silicone rubber skin were characterized and designed, respectively, to improve speed and traction performance.

A. SMA Selection and Characterization

The robot design is highly constrained by actuator choice. The primary technologies used as actuators in worm-like or peristaltic small robots are DC motors, pressurized air and Shape Memory Alloy (SMA) springs. SMA springs provide the highest energy density for miniature actuators [14]. This allows for small robots to accommodate several parallel

actuators enabling for orientation and translation degrees of freedom to be actively controlled. Both DC motors and pressurized air actuators have low power density for small weights. This imposes larger actuator sizes and weight that reduces the available space in the robot to accommodate a tool port or parallel actuators to actively control different degrees of freedom. NiTi SMA springs (2.54 mm outer diameter Flexinol[®] actuator spring) were selected [15].

SMA springs have been used to miniaturize actuators [16]. Menciassi, A et al. designed and tested a robot able to perform a worm-like motion without orientation control [17], Reza, A et al. developed a robotic section incorporating closed-loop control for orientation [18]. SMA-actuated robots use commercially available compression springs, meshed tubes or antagonistic actuators to provide the recovery force needed for the springs to expand back in their cold state [18], [19], [20]. To the authors' knowledge, no studies have been published on the design optimization of the robotic skin providing the SMA spring recovery force. In this work we design the robot skin to provide maximum robot traction balanced against providing the necessary recovery force. Finally, previous studies have shown that SMA springs have their actuation speed limited by their cooling rate [21]. Here, forced convection is implemented to reduce the SMA springs cooling process.

We have experimentally characterized the force-elongation response of the SMA springs used in this work. The experimental characterization has been used to fit Tanaka's et al. model [22] to be able to predict the spring response for a continuum of temperatures.

Initially, in Tanaka's model, all wound spring wire is in its initial phase, which is a combination of martensite and austenite. Then, for a given spring elongation, the stress at the radius of the spring wire reaches a critical stress k , which depends on the temperature and the loading or unloading state. Tanaka suggests that the critical stress can be computed as follows.

$$k_l = \tau_m = c_m(T - M_s) \quad (1)$$

$$k_u = \tau_a = c_a(T - M_a) \quad (2)$$

Where $M_s = 47.9 C^\circ$ and $M_a = 74.1 C^\circ$ are the martensitic start temperature and the austenite start temperature, respectively. And c_m and c_a are two constants to be determined experimentally.

Once the critical stress is reached, a Stressed Induced Martensitic (SIM) transformation begins at the wire radius. If the spring elongation increases, the SIM transformation propagates inwards to the center of the wire. Using a non-linear elastic material characterization approach, the spring loading process can be modeled as follows, when the SIM transformation does not progress:

$$P = \frac{dG\delta}{8D^3N}. \quad (3)$$

And, when the SIM transformation occurs:

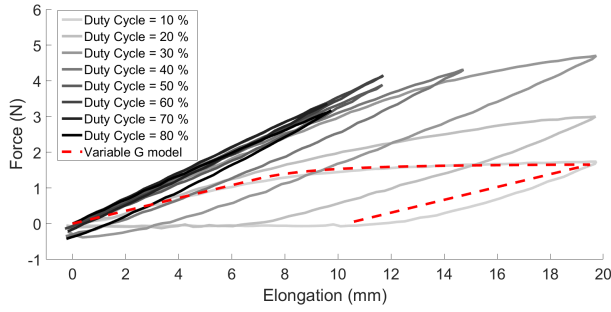


Fig. 3. Force-elongation response of the NiTi Flexinol[®] SMA spring, measured with the MTS machine, for different duty cycles. In red, Tanaka's predicted response for a 10% duty cycle input signal using the variable G model proposed in this work.

$$P = \frac{\pi k d^3}{6D} \left\{ 1 - \frac{1}{4} \left(\frac{\pi D^2 N k}{d \delta G} \right)^3 \right\}. \quad (4)$$

Where $d = 0.381$ mm is the wire diameter, $D = 2.54$ mm is the outer diameter of the spring, G is the shear modulus of the initial phase, to be determined experimentally, and $N = 15$ is the number of spring coils.

A loading-unloading test is designed to characterize the spring response. The test begins with the SMA spring at its memorized position, this being its entirely compressed state. Then, the microcontroller sends, through a power board, a PWM current signal with duty cycle d to the spring for 30 s. Based on previous tests, in 30 seconds the spring has reached an equilibrium temperature. The temperature is continuously measured during the test with a type T thermocouple attached to the spring by a high thermal conductivity, two part epoxy (OMEGABOND[®] 200). After 30 s, the Material Testing System (MTS) machine elongates the spring 20 mm at a speed of 3 mm/s and then immediately returns to its original position at the same speed while measuring the spring force response. Finally, the spring is left to rest for 3 minutes to return to ambient temperature before changing the duty cycle to perform the next test. The force is measured with a 5 N load cell being almost twice the largest force we will require from each of the springs. For high spring temperatures, if the spring is elongated 20 mm it will largely exceed 5 N. For that reason, for high temperatures the loading-unloading procedure is performed up to lower elongations and, consequently, the testing times are shorter. Figure 3 presents the experimental force-elongation curves obtained.

The presented force-elongation results show that, for the tested temperatures, no inverse SIM transformation is observed. Therefore, c_a is assumed to be zero. On the other hand, c_m can be computed using the first three duty cycles (10%, 20%, 30%) where the hysteresis cycle can be clearly observed. Finding the last point on the loading process where a linear fit would fit the data with an $R^2 \geq 0.95$ we concluded $c_m = 6.1 \text{ GPa}/^\circ\text{C}$. The shear modulus G depends on the martensitic and austenitic fraction of the initial phase, which depends on the spring temperature. By controlling the spring temperature we will be able to control

the spring stiffness and, for a given elongation, the provided force. A potential model with saturation accurately describes the G change with respect to temperature ($R^2 = 0.96$). An example of this curve fit is shown in Figure 3 for a duty cycle of 10%.

$$\begin{aligned} G &= -1136T^{-0.9926} + 38.52 & \text{if } T < 178^\circ\text{C} \\ G &= 31.9 & \text{if } T \geq 178^\circ\text{C} \end{aligned} \quad (5)$$

B. Skin Design

The robot skin is designed to maximize traction with the bowel walls while providing sufficient recovery force for the SMA springs to expand back to their original state. Traction with the bowel wall is provided by the interlocking between the robot skin and the wall. The deeper the indentation of the bowel, the greater the traction forces between the robot and the tissue. Therefore, the robot skin is designed to maximize its radial expansion when longitudinally compressed. A parametric Finite Element Analysis (FEA) study on the skin geometry is performed to evaluate the effect of the skin curvature and wall thickness on radial expansion. Figure 4 presents a general cross-section view with geometric parameters evaluated. We use Abaqus FEA software to simulate skin performance. We model the skin material as a linear elastic material with a Young Modulus of 82.7 kPa, obtained from the Ecoflex[®] 00-50 datasheet. The simulation starts with the skin at its natural elongated position. On the next step, a 24 mm displacement is imposed to the top of the skin section, representing SMA spring contraction. Then, we evaluate the radial expansion for each of the geometric configurations. Figure 5 presents the radial expansion results for the simulated configurations. For all thicknesses, $X = 8$ mm provides the largest radial expansion.

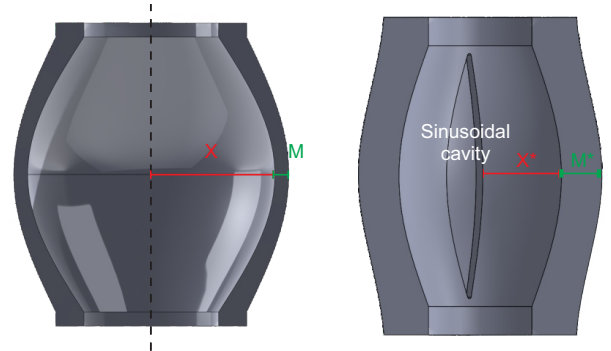


Fig. 4. On the left: Sectional view with the evaluated parameters. X is the amplitude of the inner sinusoidal skin and M is the middle section thickness. On the right: Final robot skin displaying one out of three sinusoidal cavities, $X^* = 8$ mm and $M^* = 4$ mm.

Since PCBs are mounted between robot sections, skin deformation in the shape of a clamped-clamped Euler beam is desired. This leads to a sinusoidal skin shape. Skin design goals include: 1) minimizing skin radius, X , for bowel insertion, 2) maximizing radial expansion to contact bowel walls for traction, and 3) maximizing skin wall thickness, M , for maximum restoring force. An increase in wall thickness

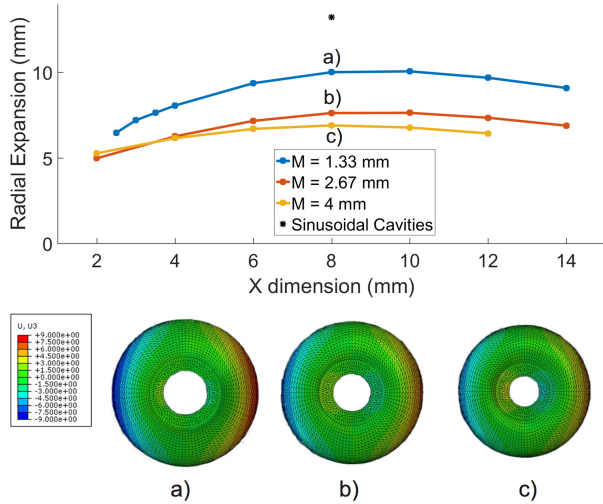


Fig. 5. Results of the skin compression FEA simulations for each of the X and M parameters evaluated. Points a), b) and c) correspond, for each middle thickness, to the maximum radial expansion. At the bottom of the image the top view of the deformed skin is presented corresponding to points a), b) and c). The black mark corresponds to the deformation achieved by the skin with sinusoidal cavities.

causes a decrease in radial expansion. This is the result of an increase of the resulting tangential force at the middle of the section when the thickness increases. The recovery force provided by the skin is positively related to the wall thickness. The SMA characterization allows us to predict that, when heated to its austenitic phase, the three springs will provide approximately 4N of force when its length is 10 mm. To generate a 4N force for a skin elongation close to 10 mm, a sinusoidal skin with 4 mm thick walls is needed, even though this sacrifices some radial expansion.

In order to increase the radial expansion we decided to reduce the radial stiffness of the skin adding three sinusoidal cavities (small radial cuts) separated 120° from each other as shown in Figure 8. This novel feature maintains structural stiffness while allowing for larger tangential deformations at the center of the section and therefore higher radial expansion.

III. ROBOT CONTROL

Closed loop control of SMA-actuated robots has been broadly studied during the last couple of decades [23], [24]. However, the complex non-linear response of the SMA springs as a function of the input current signal requires an extensive experimental characterization of the complete system which is out of the scope of this project. Researchers have been able to overcome this uncertainty by using fuzzy control techniques for their controller design [18]. Encouraged by the good results obtained using fuzzy control, a Multi Input Multi Output (MIMO) controller based on a Single Input Single Output (SISO) controller and a linearized inverse kinematic model has been designed for both of the rotational degrees of freedom, roll (θ) and pitch (ϕ). Figure

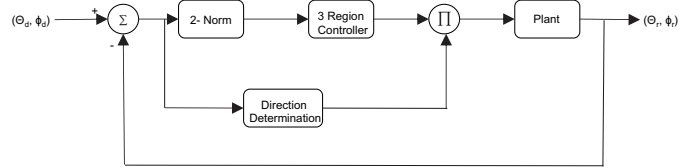


Fig. 6. Block Diagram of the MIMO control system.

6 presents the block diagram for the MIMO system. The fuzzy control has the 2-norm of the angular error vector as its input, and provides a total duty cycle to be distributed between the three springs as its output.

Three categories are selected for the fuzzy controller. Two for small errors where the controller is designed to avoid overshoot and avoid steady-state error, and one for large errors where speed response is the main feature to maximize. All three categories and their corresponding control transfer functions $D(s)$ in the Laplace space are experimentally determined. A windup release is also implemented to avoid excessive integral contribution to the controller, which could potentially destabilize the system. The integral contribution is limited to a 40% duty cycle, which corresponded to twice the duty cycle needed to maintain a 60° orientation without external disturbances. If θ_d refers to the desired angle, θ_r to the measured angle and $e = \|\theta_d - \theta_r\|$ to the norm of the error signal, the final control system can be described as:

$$D(s) = \begin{cases} 8 & \text{if } e \geq 3^\circ \\ 8 + 20s & \text{if } 2^\circ \leq e < 3^\circ \\ 8 + 20s + \frac{1.5}{s} & \text{if } e \leq 2^\circ \end{cases} \quad (6)$$

The distribution of the current signal is obtained from a linearized inverse kinematic model of the system. Figure 7 presents an schematic of the modeled system.

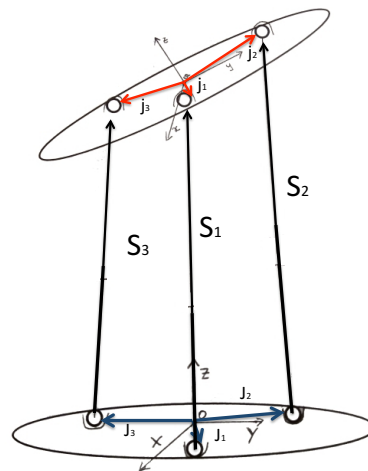


Fig. 7. Schematic of the robotic section with the notation used to deduce the inverse kinematic model of the system.

In general, assuming no translation on the $x - y$ plane is allowed, the position vector of each of the three springs can be computed as follows:

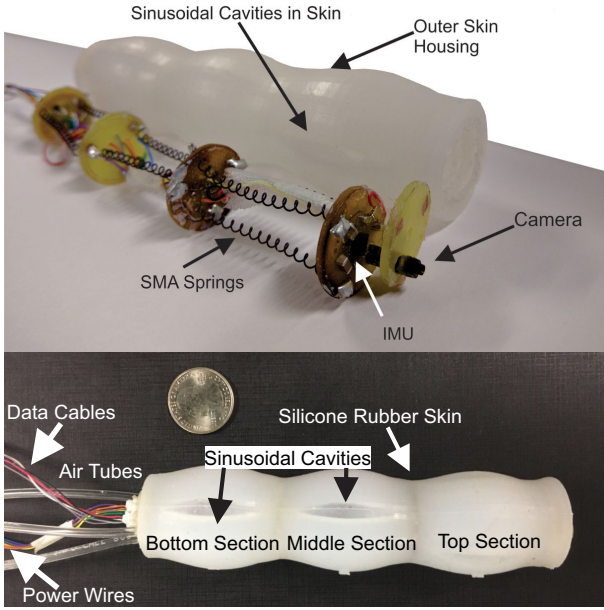


Fig. 8. Top image: Internal structure together with outer skin of the biomimetic robot. Bottom image: Assembled biomimetic robot with air tubes for force convection with quarter for scale.

$$\begin{aligned} \mathbf{S}_1 &= (0, 0, t_z) + \mathbf{q}j_1\mathbf{q}^* - J_1 \\ \mathbf{S}_2 &= (0, 0, t_z) + \mathbf{q}j_2\mathbf{q}^* - J_2 \\ \mathbf{S}_3 &= (0, 0, t_z) + \mathbf{q}j_3\mathbf{q}^* - J_3 \end{aligned} \quad (7)$$

Where \mathbf{q} is a quaternion defining the orientation of the top platform, movable frame, with respect to a fixed frame on the bottom platform, t_z is the platform vertical displacement, j_i is the position vector expressed on the movable frame of the end point of the i spring, and J_j is the position vector on the fixed frame of the initial point of the j spring.

Introducing vectors j_i and J_j for our system and linearizing the rotation quaternion \mathbf{q} , we derive a simplified inverse kinematic model for our system.

$$\begin{aligned} \mathbf{S}_1 &= (0, 0, t_z) + 7.62(0, 0, -\phi) \\ \mathbf{S}_2 &= (0, 0, t_z) - 3.81(0, 0, -\phi) + 6.6(0, 0, \theta) \\ \mathbf{S}_3 &= (0, 0, t_z) - 3.81(0, 0, -\phi) - 6.6(0, 0, \theta) \end{aligned} \quad (8)$$

For a given error (e_θ, e_ϕ) the required change in S_1 , S_2 and S_3 is computed. If S_i is determined to be negative it is zeroed as we cannot actively provide expansion forces. The total duty cycle is then distributed in the direction of change $(S_1, S_2, S_3) / \sum_{i=1}^3 S_i$. The controller performance on the biomimetic soft robot is presented in the Results section.

IV. BIOMIMETIC MODULAR ROBOT DESIGN

A three section biomimetic robot has been designed and built incorporating the skin design and the MIMO controller for each of the sections. The desired skin profile is fabricated molding Ecoflex[®] 00-50 with a customized mold. The mold has been designed with SolidWorks and fabricated using an Objet30 printer. The complete robot design with the internal components and the functional skin is presented in Figure 8.

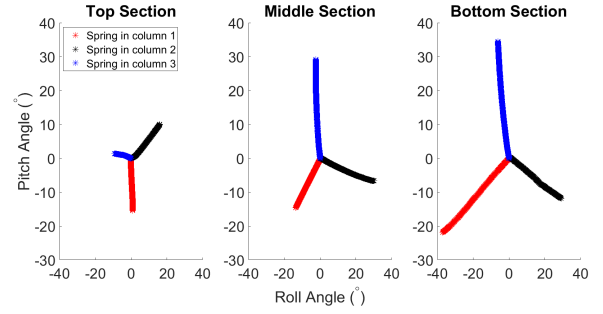


Fig. 9. Change in orientation when a single spring is activated for 10 seconds with a 50% duty cycle signal. For a perfect set-up we would expect, for each section, equal change in orientation magnitude independently of the activated spring. The calibration is performed vertically which explains the more substantial orientation change when activating the middle and bottom sections. The calibration reflects the 120° symmetry in each section and the 60° rotation between the top section and the other two sections.

To improve the orientation performance a calibration process is performed for the controller to obtain the matrix relating the rotation angles and the spring elongation. This calibration is performed to correct for manufacturing irregularities and so that the first order approximation used in our control strategy is as accurate as possible. The calibration process consists on applying a 50% duty cycle signal to each of the springs and evaluate the change in orientation of the top platform as measured by the IMU. The experimental results are presented in Figure 9. If we note as r_{ij} and p_{ij} the change in roll and pitch angle respectively caused by the activation of the spring in section i and column j , the following linearized system expressed in Einstein notation is obtained.

$$\begin{pmatrix} \theta \\ \phi \end{pmatrix} = \begin{pmatrix} r_{i,j} s_{i,j} \\ p_{i,j} s_{i,j} \end{pmatrix} \quad (9)$$

Where s_{ij} is the change in elongation of the spring in section i and column j . The r_{ij} and p_{ij} experimentally obtained are the following ones.

$$\begin{aligned} \begin{pmatrix} \theta \\ \phi \end{pmatrix} &= \begin{pmatrix} 0.063 & 0.849 & -0.989 \\ -0.998 & 0.528 & 0.147 \end{pmatrix} \begin{pmatrix} s_{11} \\ s_{12} \\ s_{13} \end{pmatrix} + \\ &+ \begin{pmatrix} -0.680 & 0.976 & -0.081 \\ -0.734 & -0.217 & 0.997 \end{pmatrix} \begin{pmatrix} s_{21} \\ s_{22} \\ s_{23} \end{pmatrix} + \\ &+ \begin{pmatrix} -0.862 & 0.927 & -0.175 \\ -0.508 & -0.375 & 0.985 \end{pmatrix} \begin{pmatrix} s_{31} \\ s_{32} \\ s_{33} \end{pmatrix} \end{aligned} \quad (10)$$

The calibrated controller system has been used to evaluate the orientability of the robot. Periodic multi input signals going up to 25° in amplitude, both for roll and pitch angles, have been evaluated. In Figure 10 an image of the robot achieving the desired orientation by controlling each of the three sections is presented.

Finally, the robot has been programmed to perform a peristaltic motion. The peristaltic motion is achieved by compressing the robotic sections, activating the three SMA springs, and expanding the robotic sections, cooling the

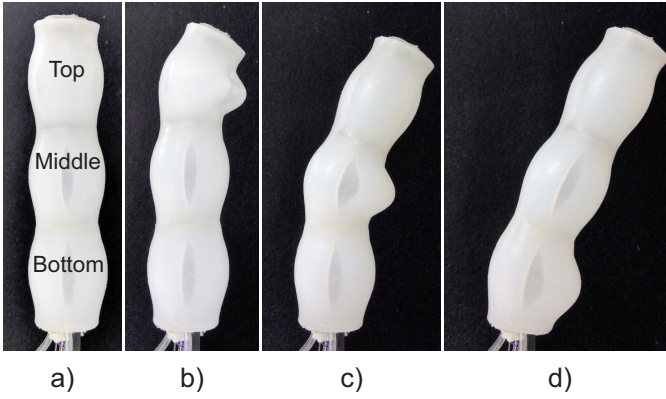


Fig. 10. In a) the soft robot is in its natural state, in b) the top section is controlled to obtain a 30° rotation. In c) the middle section is controlled to obtain a 30° rotation and in d) the bottom section is controlled to change the orientation of the tip of the robot by 30° .

TABLE I

SINGLE PERIOD OF THE ACTUATION SEQUENCE FOLLOWED TO PERFORM THE PERISTALTIC MOTION. SECTIONS ARE COMPRESSED BY ACTIVATING THE THREE SMA SPRINGS. SECTIONS ARE PASSIVELY EXPANDED BY THE ROBOT SKIN WHILE THE SMA SPRINGS ARE COOLED USING FORCED CONVECTION.

Step	Top Section	Middle Section	Bottom Section
1	Compress	Inactive	Expand
2	Inactive	Compress	Inactive
3	Expand	Inactive	Compress
4	Inactive	Expand	Compress

springs using forced convection, in a programmed sequence. In Table I the actuation sequence followed to generate the peristaltic motion is summarized.

V. RESULTS

A. Skin Design

The FEA parametric study allowed for the design of a skin improving the traction response by increasing the radial expansion while being sufficiently stiff to expand the SMA springs back to their original state. The resulting sinusoidal skin with sinusoidal cavities proved, both in simulations and experimentally, to largely expand radially when longitudinally compressed while being four times stiffer than a no-cavity skin ($M = 1.33$ mm) able to radially expand as much. Figure 11 shows the improved performance of the sinusoidal skin with cavities versus the skin without cavities.

B. Biomimetic Robot

A soft 2.4 cm diameter 13.9 cm long biomimetic robot has been designed, modeled, built and tested. The ability of the robot to arbitrarily orient has been tested on nine MIMO squared signals going from -25° to 25° both in pitch and roll, three for each section. Its availability to generate a peristaltic motion has been tested in a 4 cm diameter tube.

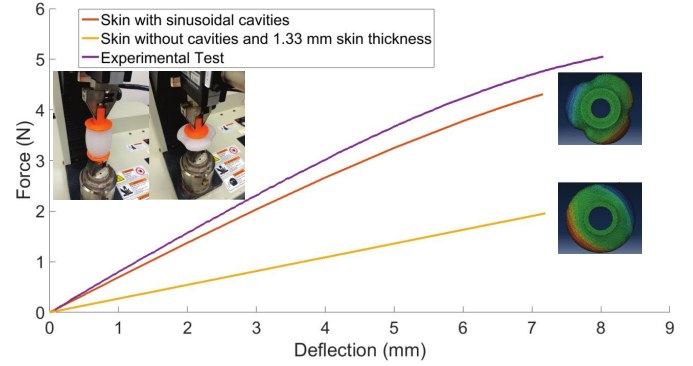


Fig. 11. Force-displacement response for a 4 mm thick skin with sinusoidal cavities versus a 1.33 mm thick skin without cavities. Together with the simulation and experimental images of the radial expansion for each of the configurations.

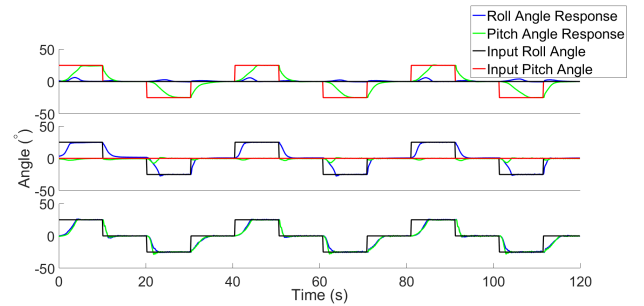


Fig. 12. Biomimetic robot response to three different input signals. From top to bottom, robot response to a periodic signal controlling: the top section, the middle section and the bottom section.

TABLE II

SUMMARY OF PARAMETERS EVALUATING THE MIMO CONTROLLER PERFORMANCE

	Mean	Standard Deviation
M_p (%)	1.81	2.78
t_r (s)	2.07	0.66
t_s (s)	3.80	0.91
e_{ss} (%)	0.83	0.7

1) *Orientation Control*: Figure 12 presents a sample of the biomimetic robot response to three MIMO periodic inputs applied to the top, middle and bottom robotic sections.

Table II summarizes the transient response of the nine non-zero squared periodic signals tested. When forced convection is deactivated, the section is unable to perform more than three cycles given that, at that point in time, the three springs in the section would be completely compressed. The use of forced convection allows the response to be faster and allows for continue cycling.

2) *Peristaltic Motion*: Figure 14 shows the robot advance in a transparent 4 cm outer diameter PVC tube. The designed robot has proved to be able to reproduce the peristaltic motion moving 15 cm in 6 minutes. The use of forced convection has proved to be essential as, when the same test

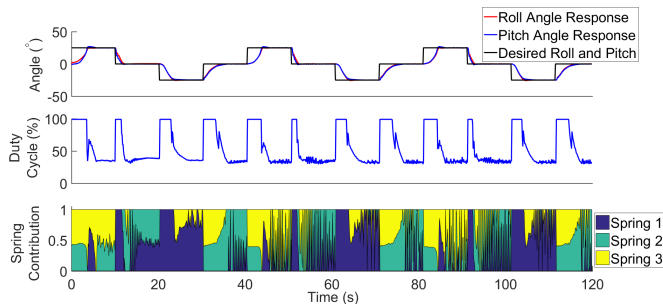


Fig. 13. Orientation performance when using the middle section to control the orientation of the tip of the robot. From top to bottom: angular response of the robot, total duty cycle applied to the three springs, distribution of the duty cycle to each of the springs.

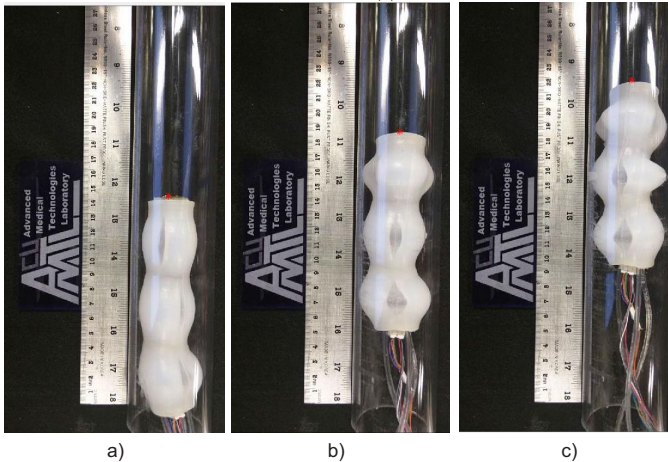
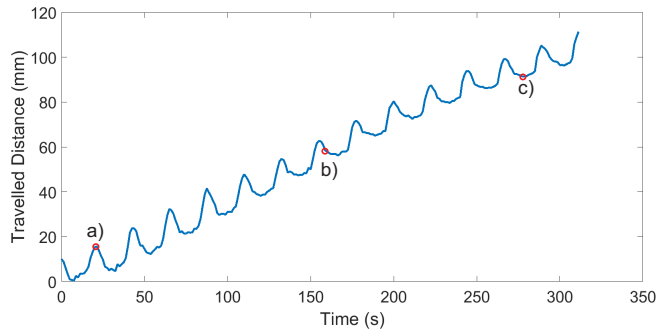


Fig. 14. Biomimetic robot peristaltic motion for displacement. The top graph displays the travel of the tip of the robot along the tube. The robot state at points a), b) and c) is presented in the images below the plot. In a) the bottom section is compressed while the top and middle are expanded. In b) the top section gets compressed while the bottom gets expanded. In c) the three sections are compressed.

is performed without forced convection, it takes three times as long to move the same distance.

VI. CONCLUSIONS

In this work a nine degree of freedom soft biomimetic robot is designed, modeled, and fabricated. Two main features are incorporated in the robot design to improve its mobility. First, a novel silicone rubber skin is designed to increase the robot traction while providing sufficient recovery force for the SMA springs. Second, forced convection is

implemented at every robotic section reducing the cooling time of the SMA springs. Those features have proven to drastically improve the robot speed and orientation capabilities. In addition, the use of the skin as a functional element allows for the interior of the robot to be empty, which could be used to incorporate a tool port. This soft robot design also contains a camera for visual feedback.

Additionally, a MIMO controller inspired by fuzzy control and a linearized inverse kinematic model is implemented and tested. The robot design and MIMO controller implementation have been tested in a controlled laboratory setting proving fast and precise orientability and the ability to perform a peristaltic motion.

VII. FUTURE WORK

Future work will continue exploring the use of the robot skin as a functional element. *In vivo* testing of the biomimetic robot would provide experimental data of its performance in a more realistic environment. The skin will also be redesigned to improve the forced convection system. In our design, the air started flowing in the desired section but is allowed to flow through the other sections. Consequently, the heating time of other sections is increased.

The incorporation of two more IMUs in the robot will allow for the orientation control of each of the sections separately. Additionally, the incorporation of soft pressure sensors on the skin could be used as an additional information source to detect abnormalities while exploring the large bowel. Finally, the use of the camera feedback to autonomously guide the biomimetic robot would further simplify the procedure.

ACKNOWLEDGMENT

This research was supported in part by the National Science Foundation (NSF) (Grant No. 1235532), the Balsells Graduate Fellowship Program and the Beverly Sears Graduate Student Grant program.

REFERENCES

- [1] R. L. Siegel, K. D. Miller, and A. Jemal, "Cancer statistics, 2015," *CA: a cancer journal for clinicians*, vol. 65, no. 1, pp. 5–29, 2015.
- [2] J. B. Marshall, "Technical proficiency of trainees performing colonoscopy: a learning curve," *Gastrointestinal endoscopy*, vol. 42, no. 4, pp. 287–291, 1995.
- [3] N. M. Gatto, H. Frucht, V. Sundararajan, J. S. Jacobson, V. R. Grann, and A. I. Neugut, "Risk of perforation after colonoscopy and sigmoidoscopy: a population-based study," *Journal of the National Cancer Institute*, vol. 95, no. 3, pp. 230–236, 2003.
- [4] D. Cave, P. Legnani, R. De Franchis, and B. Lewis, "Icece consensus for capsule retention," *Endoscopy*, vol. 37, no. 10, pp. 1065–1067, 2005.
- [5] L. J. Sliker, M. D. Kern, J. A. Schoen, and M. E. Rentschler, "Surgical evaluation of a novel tethered robotic capsule endoscope using micro-patterned treads," *Surgical endoscopy*, vol. 26, no. 10, pp. 2862–2869, 2012.
- [6] R. J. W. I. J. L. Gorlewicz and P. Valdastri, "Mesoscale mobile robots for gastrointestinal minimally invasive surgery (mis)," *Woodhead Publishing*, 2012.
- [7] B. Vucelic, D. Rex, R. Pulanic, J. Pfefer, I. Hrstic, B. Levin, Z. Halpern, and N. Arber, "The aer-o-scope: proof of concept of a pneumatic, skill-independent, self-propelling, self-navigating colonoscope," *Gastroenterology*, vol. 130, no. 3, pp. 672–677, 2006.

- [8] K. Kong, D. Jeon, S. Yim, and S. Choi, "A robotic biopsy device for capsule endoscopy," *Journal of Medical Devices*, vol. 6, no. 3, p. 031004, 2012.
- [9] G. Ciuti, R. Donlin, P. Valdastrì, A. Arezzo, A. Menciassi, M. Morino, P. Dario *et al.*, "Robotic versus manual control in magnetic steering of an endoscopic capsule," *Endoscopy*, vol. 42, no. 2, p. 148, 2010.
- [10] B. Kim, H.-Y. Lim, K.-D. Kim, Y. Jeong, and J.-O. Park, "A locomotive mechanism for a robotic colonoscope," in *Intelligent Robots and Systems, 2002. IEEE/RSJ International Conference on*, vol. 2. IEEE, 2002, pp. 1373–1378.
- [11] M. Simi, P. Valdastrì, C. Quaglia, A. Menciassi, and P. Dario, "Design, fabrication, and testing of a capsule with hybrid locomotion for gastrointestinal tract exploration," *IEEE/ASME Transactions on Mechatronics*, vol. 15, no. 2, pp. 170–180, 2010. [Online]. Available: <http://ieeexplore.ieee.org/lpdocs/epic03/wrapper.htm?arnumber=5420046>
- [12] K. Wang, Y. Ge, and X. Jin, "A micro soft robot using inner air transferring for colonoscopy," in *Robotics and Biomimetics (ROBIO), 2013 IEEE International Conference on*. IEEE, 2013, pp. 1556–1561.
- [13] R. Mukherjee, T. F. Christian, and R. A. Thiel, "An actuation system for the control of multiple shape memory alloy actuators," *Sensors and Actuators A: Physical*, vol. 55, no. 2, pp. 185–192, 1996.
- [14] K. Ikuta, "Micro/miniature shape memory alloy actuator," in *Robotics and Automation, 1990. Proceedings., 1990 IEEE International Conference on*. IEEE, 1990, pp. 2156–2161.
- [15] W. Huang, "On the selection of shape memory alloys for actuators," *Materials and design*, vol. 23, no. 1, pp. 11–19, 2002.
- [16] A. Nespoli, S. Besseghini, S. Pittaccio, E. Villa, and S. Viscuso, "The high potential of shape memory alloys in developing miniature mechanical devices: A review on shape memory alloy mini-actuators," *Sensors and Actuators A: Physical*, vol. 158, no. 1, pp. 149–160, 2010.
- [17] A. Menciassi, D. Accoto, S. Gorini, and P. Dario, "Development of a biomimetic miniature robotic crawler," *Autonomous Robots*, vol. 21, no. 2, pp. 155–163, 2006.
- [18] R. Abiri, R. Nadafi, and M. Kabganian, "Design, fabrication, and nonlinear control of a flexible minirobot module by using shape memory alloy actuators," *Journal of Intelligent Material Systems and Structures*, p. 1045389X15590638, 2015.
- [19] S. Seok, C. D. Onal, K.-J. Cho, R. J. Wood, D. Rus, and S. Kim, "Meshworm: a peristaltic soft robot with antagonistic nickel titanium coil actuators," *IEEE/ASME Transactions on mechatronics*, vol. 18, no. 5, pp. 1485–1497, 2013.
- [20] S. Kim, E. Hawkes, K. Choy, M. Joldaz, J. Foley, and R. Wood, "Micro artificial muscle fiber using niti spring for soft robotics," in *2009 IEEE/RSJ International Conference on Intelligent Robots and Systems*. IEEE, 2009, pp. 2228–2234.
- [21] K. Ikuta, "Micro/miniature shape memory alloy actuator," in *Robotics and Automation, 1990. Proceedings., 1990 IEEE International Conference on*. IEEE, 1990, pp. 2156–2161.
- [22] H. Tobushi and K. Tanaka, "Deformation of a shape memory alloy helical spring (analysis based on stress-strain-temperature relation)," *JSME international journal. Series 1, solid mechanics, strength of materials*, vol. 34, no. 1, pp. 83–89, 1991.
- [23] N. Ma, G. Song, and H. Lee, "Position control of shape memory alloy actuators with internal electrical resistance feedback using neural networks," *Smart materials and structures*, vol. 13, no. 4, p. 777, 2004.
- [24] G. V. Webb, D. C. Lagoudas, and A. J. Kurdila, "Hysteresis modeling of sma actuators for control applications," *Journal of Intelligent Material Systems and Structures*, vol. 9, no. 6, pp. 432–448, 1998.